

Article

Removal of Bisphenol A from Water by Single-Walled Carbon Nanotubes Loaded with Iron Oxide Nanoparticles

Luying Chen ^{1,2}, Jintao Jiang ³ and Leimei Sheng ^{1,2,*}¹ School of Physics, Shanghai University, Shanghai 200444, China; 3146617397@shu.edu.cn² Institute of Low-Dimensional Carbon and Device Physics, Shanghai University, Shanghai 200444, China³ School of Materials Science and Engineering, Shanghai University, Shanghai 200444, China; jiangjintao1102@shu.edu.cn

* Correspondence: shenglm@staff.shu.edu.cn

Abstract: Single-walled carbon nanotubes (SWCNTs) loaded with magnetic iron oxide nanoparticles were prepared by the arc discharge method and air heat treatment. The nanocomposite was characterized by X-ray diffraction, scanning electron microscopy, Raman spectroscopy, vibrating sample magnetometry, etc. The results showed that the heat-treated nanocomposites (SWCNTs/Fe_xO_y) had iron oxide phases and superparamagnetic properties with a saturation magnetization of 33.32 emu/g. Compared with the non-heat-treated materials, SWCNTs/Fe_xO_y had a larger specific surface area and pore volume. Using SWCNTs/Fe_xO_y to remove the organic contaminant (bisphenol A, BPA), it was found that under the conditions of pH = 3 and adsorbent dosage of 0.2 g/L, the maximum adsorption capacity of the composite was 117 mg/g, and the adsorption could reach more than 90% in only 5 min when the BPA content was below 0.05 mmol/L. The fitting results of the Langmuir and D-R models are more consistent with the experimental data, indicating a relatively uniform distribution of the adsorption sites and that the adsorption process is more consistent with physical adsorption. The kinetic calculations showed that the SWCNTs/Fe_xO_y exhibits chemical effects on both the surface and the gap, and the adsorption process is controlled by the π - π bonds and the hydrophobicity of the SWCNTs/Fe_xO_y.

Keywords: SWCNT composites; Bisphenol A; magnetic iron oxide nanoparticles; adsorption; adsorption mechanism



Citation: Chen, L.; Jiang, J.; Sheng, L. Removal of Bisphenol A from Water by Single-Walled Carbon Nanotubes Loaded with Iron Oxide Nanoparticles. *Appl. Sci.* **2024**, *14*, 3943. <https://doi.org/10.3390/app14093943>

Academic Editor: Piotr Gas

Received: 24 March 2024

Revised: 23 April 2024

Accepted: 1 May 2024

Published: 6 May 2024



Copyright: © 2024 by the authors. Licensee MDPI, Basel, Switzerland. This article is an open access article distributed under the terms and conditions of the Creative Commons Attribution (CC BY) license (<https://creativecommons.org/licenses/by/4.0/>).

1. Introduction

In recent years, with the rapid development of industrialization, the problem of water pollution has become increasingly prominent. The pollutants of concern include bisphenol A (BPA), a ubiquitous chemical widely used in the production of plastics and resins. However, BPA is a quintessential endocrine disruptor in the environment [1] and can disrupt the normal physiological functions of the human body even in minute quantities. Numerous studies have revealed that BPA enters the human body through various common pathways, such as contaminating water, food, cooking fumes, and even through daily direct contact, posing threats to human health and affecting estrogen levels. The extensive production and use of BPA has led to its widespread presence in the environment, and it has even been detected in drinking water [2–4]. Currently, numerous technologies have been developed to eliminate BPA, including advanced oxidation processes, biodegradation, membrane separation, adsorption [5–8], and more. In fact, a large number of researchers believe that adsorption [9,10] is better than other methods, as it can quickly and effectively adsorb pollutants. Additionally, adsorption offers advantages such as cost-effectiveness, efficiency, simple design, and fewer harmful by-products.

With their exceptional adsorption efficacy, various carbon materials [11], such as graphene oxide (GO), activated carbon (AC), and carbon nanotubes (CNTs) [12–15], have been increasingly adopted as preferred adsorbents for the eradication of contaminants

from aquatic environments. Among them, CNTs [16], as a new adsorbent material, have been used in many studies [17] to adsorb pollutants in water owing to their extensive surface area and plentiful reactive sites. Evidence confirms that CNTs possess a strong capacity to adsorb phenols, heavy metals, and natural organic compounds effectively [18]. Nevertheless, the isolation of CNTs from suspension in aqueous media poses a challenge because of their minute dimensions, and their introduction into water resources may result in secondary pollution [19]. On the other hand, magnetic nanoparticles such as Fe_3O_4 , $\gamma\text{-Fe}_2\text{O}_3$, and Fe^0 have drawn considerable interest due to their excellent adsorption characteristics [20,21], and their inherent superparamagnetism enables them to be readily extricated from aqueous environments using magnetic attraction after application. The practical usage of magnetic nanoparticles often faces issues like pronounced clustering in suspension and a susceptibility to being lost via water runoff. Therefore, CNTs are usually used as a carrier [22,23] to support magnetic nanoparticles such as Fe_3O_4 and Fe^0 , and their superparamagnetism [24] is used to enable them to effectively perform magnetic separation in water, which is not only conducive to improving the adsorption performance, but also to improving the dispersion and mechanical properties [25,26] of these magnetic nanoparticles in practical applications. For example, Li et al. [27] successfully fabricated a recyclable CNTs/ Fe_3O_4 magnetic composite via a hydrothermal method, which exhibited robust adsorption behaviors towards BPA. Al-Musawi et al. [28] synthesized multi-walled carbon nanotubes coated with CoFe_2O_4 nanoparticles using solvothermal co-precipitation and electrophoretic precipitation methods, and applied it to the adsorption of BPA in water. The experimental findings indicated that the incorporation of a composite material significantly augmented the adsorption capabilities as well as enhanced the characterization attributes of multi-walled carbon nanotubes (MWCNTs). Guo et al. [29] synthesized MWCNTs modified with iron oxide and manganese dioxide (MWCNTs- FeO-MnO) via the co-precipitation method, and utilized them to determine the levels of residual BPA in bottled water supplies. The results demonstrated that the nanotubes possessed effective adsorptive qualities for BPA, along with commendable recyclability and concentration capabilities. Most studies have focused on MWCNTs, with fewer reports on SWCNTs [30]. Nevertheless, SWCNTs exhibit superior performance; they possess smaller diameters and a larger specific surface area compared to MWCNTs. Therefore, drawing on earlier investigations into phenol elimination from water, this study prepared magnetic SWCNT composites incorporating iron oxide nanoparticles via an electric arc process followed by thermal treatment. The adsorption behavior and underlying mechanisms of the composites towards BPA were investigated. These results offer foundational theoretical and empirical support for the application of magnetic SWCNT nanocomposites in the removal of organic contaminants during water purification processes.

2. Materials and Methods

2.1. Adsorbent Preparation

We employed the hydrogen arc discharge method to fabricate SWCNTs, utilizing a carbon rod doped with 4 wt% iron as the anode and the carbon rod's composition was pure toner and iron powder; a pure graphite carbon rod was used as the cathode. Both electrodes had a diameter of 10 mm. Within the arc reaction chamber, the anode and cathode were horizontally secured at the left and right flanks, respectively, maintaining a distance of 2–3 mm [31]. Under conditions of low vacuum, a hydrogen/argon (volume ratio of 2:3) mixture gas at 200 torr pressure was introduced into the reaction vacuum chamber. With a current of 100 A, after about 30 min of arc discharge, a substantial amount of black SWCNTs containing iron catalyst adhered to the interior chamber walls. The as-grown SWCNTs of iron-containing catalyst were then heated in dry air to 350 °C and kept for 1 h. Finally, SWCNT composites loaded with magnetic iron oxide nanoparticles (SWCNTs/ Fe_xO_y) were obtained.

2.2. Adsorption Experiment

Pre-measured solid BPA particles were dissolved in deionized water to obtain BPA master solution (1 mmol/L). The master solution was further diluted with deionized water to create BPA solutions in different concentrations, adjusted the pH value of the solution by adding an appropriate amount of HCl or NaOH. Each experiment was conducted in a beaker containing 50 mL of BPA solution, with an adsorbent dosage of 10 mg (0.2 g/L). A magnetic stirrer was used to agitate the BPA solution and adsorbent at a rotational speed of 500 revolutions per minute, while the temperature for adsorption was kept constant at ambient conditions (25 °C). At predetermined time intervals, 2 mL of the suspension was extracted from the beaker and subsequently filtered utilizing a polyethersulfone (PES) membrane filter with a pore size of 0.22 μm. The residual organic compound concentration was analyzed by ultraviolet–visible–near-infrared absorption spectroscopy (UV-vis-NIR spectroscopy, UV-3600, Shimadzu, Japan). The rate of BPA adsorption α in the solution by SWCNTs/Fe_xO_y as the adsorbent and the adsorption capacity q_t as the unit mass of the adsorbent at a certain time are written as follows.

$$\alpha = \frac{C_0 - C_t}{C_t} \times 100\%, \quad (1)$$

$$q_t = \frac{(C_0 - C_t)V}{m}, \quad (2)$$

where C_0 is the concentration of BPA solution at the initial time (mmol/L); C_t is the concentration of BPA solution at time t (mmol/L); V is the volume (L) of the solution; m is the mass (g) of the adsorbent; α is the adsorption rate; and q_t is the adsorption capacity (mg/g).

2.3. Microstructure Analyses

The morphologies of the nanocomposites were observed by scanning electron microscopy on a Gemini 500 instrument (Zeiss, Oberkochen, Germany) at a magnification of 20,000–100,000.

The structural characterization of the nanocomposites was characterized using a X-ray diffractometer from Rigaku, JP, model D/max-2550. The X-ray source was Cu K α radiation, with a wavelength of 1.54056 Å and a power of 18 KW. The scanning angle range was set from 15° to 85°.

The structure of the nanocomposites was studied using a Raman spectroscope from Renishaw, UK, model In Via-plus. The Raman spectroscope was equipped with a Leica microscope. The excitation wavelength used was 633 nm.

The surface elemental composition and chemical state of the nanocomposites were analyzed using an X-ray Photoelectron Spectrometer from Thermo Fisher Scientific, Winsted, UK, model ESCALAB 250Xi. To control the surface composition of the sample, survey spectra were collected at a step size of 1 eV over the range of 0–1100 eV.

The nitrogen adsorption–desorption isotherms of the nanocomposites were measured at 77 K using a surface area and pore size distribution analyzer (ASAP2020, Micromeritics Instrument Co., Norcross, GA, USA). Before measurement, the nanocomposite samples were degassed at 105 °C for over 16 h. The specific surface area of the nanocomposites was calculated using the Brunauer–Emmett–Teller (BET) method, while the pore diameter and volume were determined from the desorption isotherm using the Barrett–Joyner–Halenda (BJH) method.

The measurement of magnetic properties was conducted using the Magnetic Property Measurement System (MPMS3) from Quantum Design, San Diego, CA, USA. In this study, measurements were carried out in VSM (Vibrating Sample Magnetometer) mode.

3. Results and Discussion

3.1. Characterization

Figure 1a shows the SEM micrograph of the as-grown SWCNTs. The image reveals that the SWCNTs, synthesized with the aid of an iron catalyst, possess a loose arrangement. The bundles of CNTs are observed to be entangled with each other, and they are coated with large amounts of amorphous carbon. The SEM image at a high magnification (Figure 1b) more clearly reveals the prepared SWCNT bundle loaded with iron nanoparticles. From the energy dispersive spectra (EDS) finding (Figure 1c), it can be seen that the region comprised 51.79 wt% C element, 6.41 wt% O element, and 41.62 wt% Fe element, indicating that the iron nanoparticles were successfully attached to the surface of the CNTs.

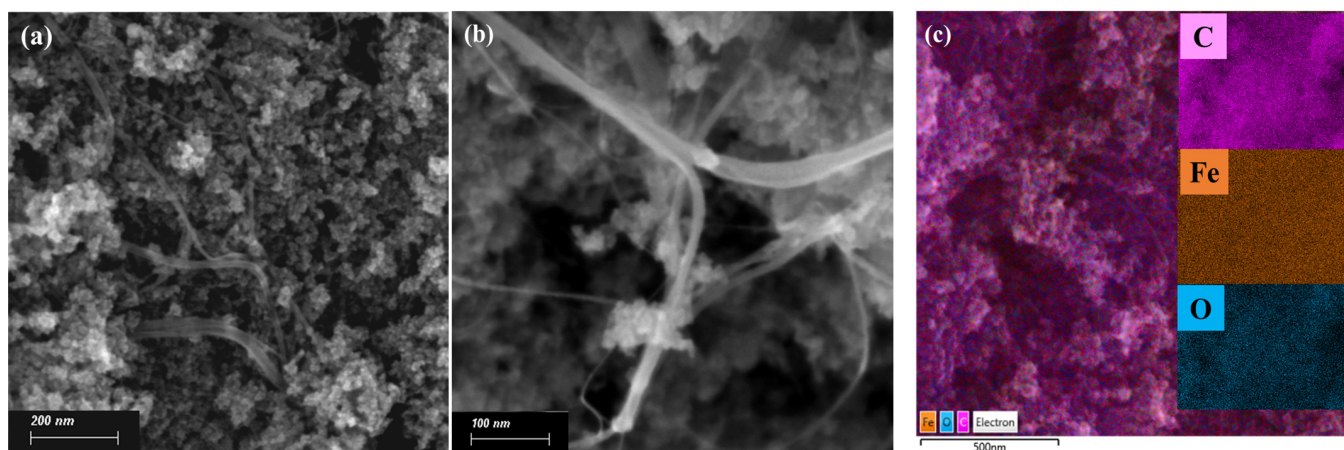


Figure 1. Scanning electron micrographs of (a) low-magnification as-grown SWCNTs and (b) high-magnification as-grown SWCNTs; (c) EDS image.

Figure 2a displays the XRD spectra of the as-grown SWCNTs and the air-heat-treated SWCNTs. It shows that the diffraction peaks of C in the as-grown SWCNTs diminish after the air heat treatment, indicating the effective removal of amorphous carbon from the composite, thereby enhancing its adsorption capacity. Simultaneously, the Fe phase is transformed into the Fe_2O_3 and Fe_3O_4 phases after heat treatment. Figure 2b depicts the Raman spectra obtained under 633 nm laser excitation for the as-grown SWCNTs and SWCNTs/ Fe_xO_y . Within the range of $100\text{--}400\text{ cm}^{-1}$, resonant breathing mode (RBM) peaks of the SWCNTs are evident, allowing for the calculation of the diameter of the SWCNTs using the frequency (ω_{RBM}) of the RBM peak. For the SWCNTs, the calculation formula is $\omega_{\text{RBM}} (\text{cm}^{-1}) = 234/d (\text{nm}) + 10$, and the diameter of the SWCNTs in the original sample ranges between 0.89 and 1.78 nm. The weak Raman peak at 1350 cm^{-1} is the D peak, which arises from defects like pentagon and heptagon rings within the CNTs, reflecting the defect density directly. The prominent Raman peak near 1590 cm^{-1} is the G peak, which is associated with in-plane tangential vibrations of carbon atoms. The intensity ratio of the D peak to the G peak ($I_{\text{D}}/I_{\text{G}}$) is typically utilized to characterize the defect content in SWCNTs; a lower ratio signals fewer defects and higher crystallinity. The $I_{\text{D}}/I_{\text{G}}$ ratio of the SWCNTs/ Fe_xO_y and as-grown SWCNTs was 0.06 and 0.2196, respectively. The findings demonstrate that the crystallinity of the sample was enhanced subsequent to the heat treatment and the D peak was significantly decreased after the air heat treatment.

Figure 3 displays the XPS spectra of SWCNTs/ Fe_xO_y (Figure 3a–c) and as-grown SWCNTs (Figure 3d–f), including the regions for Fe 2p, O 1s, and C 1s. The analysis shows that the main valence state of iron in the as-grown SWCNTs prepared by the arc discharge method exists in the form of Fe^0 , although a small amount of Fe_3C phase is formed during the arc evaporation process. After air oxidation treatment, the iron valence states in SWCNTs/ Fe_xO_y are mainly Fe^{2+} and Fe^{3+} , while a small amount of Fe^0 phase still exists, which may be due to the incomplete oxidation of Fe nanoparticles in the internal

region. It is worth noting that although the XRD analysis failed to detect the Fe^0 signal, this may be due to its low content, which is below the detection limit of X-rays.

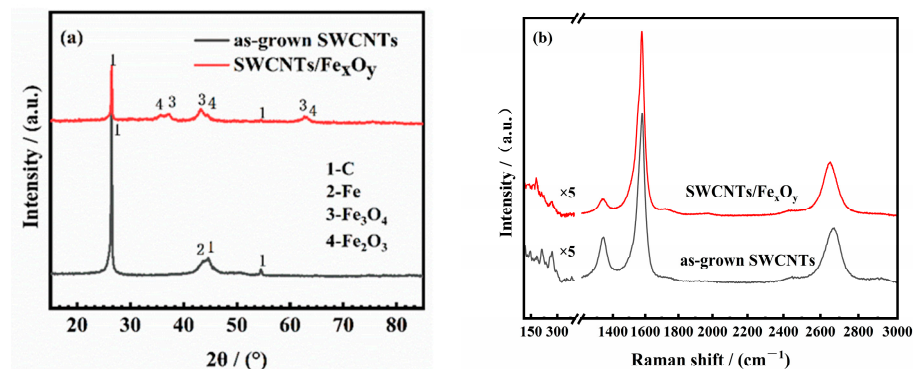


Figure 2. (a) XRD images and (b) Raman spectra of as-grown SWCNTs and SWCNTs/ Fe_xO_y .

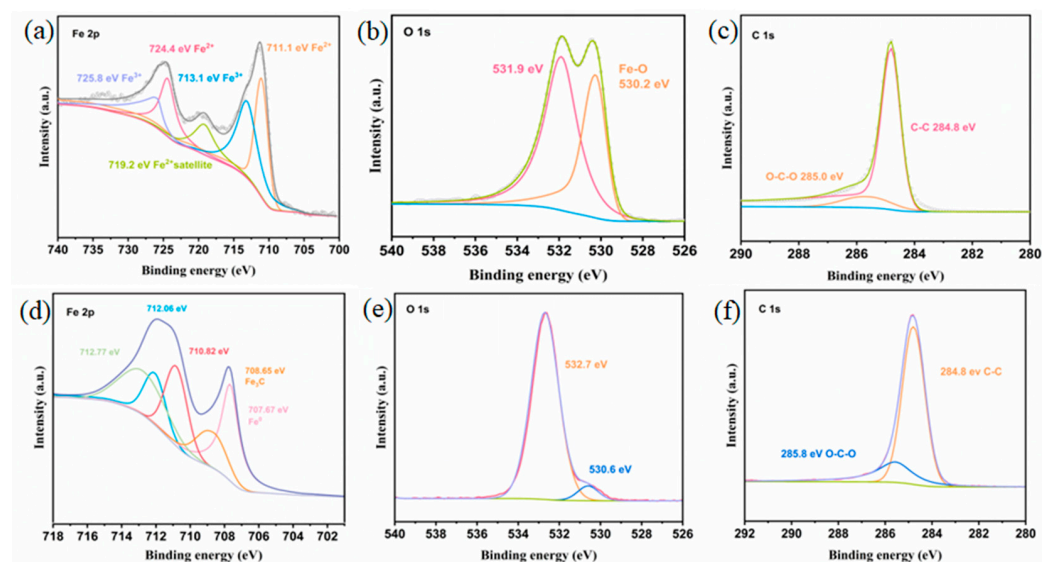


Figure 3. XPS spectra of SWCNTs/ Fe_xO_y and as-grown SWCNTs.

Figure 4 presents the N_2 adsorption–desorption curves and pore size distribution for the as-grown SWCNTs and SWCNTs/ Fe_xO_y , and the specific surface area, pore volume, and average pore diameter of the two nanocomposites are given in Table 1. As demonstrated in Figure 4 and Table 1, it appears that the adsorption–desorption isotherm exhibits an H_3 hysteresis loop, and compared to the as-grown SWCNTs, the SWCNTs/ Fe_xO_y has a larger specific surface area and pore volume and a larger pore diameter. The specific surface area of a material is determined by the synergistic contribution of micropores, mesopores, and macropores. Generally speaking, a larger capacity of micropores correlates with a higher specific surface area of the material, and when mesopores and macropores are present in significant quantities, the average pore size of the material tends to decrease. It is evident that thermal treatment effectively removes amorphous carbon, which is favorable for the formation of micropores. This not only increases the number of adsorption channels but also prolongs the adsorbate residence time within these channels due to the abundance of micropores. As a result, adsorbate molecules are more easily adsorbed onto the SWCNTs/ Fe_xO_y .

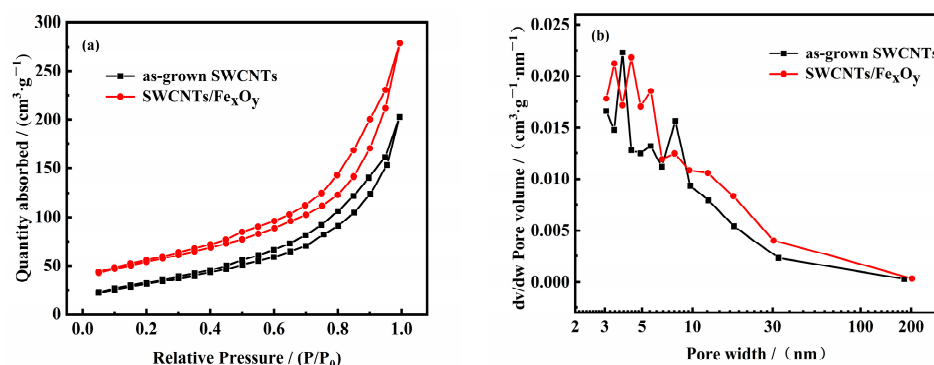


Figure 4. (a) N_2 adsorption–desorption curves and (b) pore size distribution of as-grown SWCNTs and SWCNTs/ Fe_xO_y .

Table 1. Pore structure analysis of SWCNTs/ Fe_xO_y and as-grown SWCNTs.

| Sample | BET $m^2 \cdot g^{-1}$ | Pore Volume $cm^3 \cdot g^{-1}$ | Pore Diameter nm |
|-------------------|---------------------------|------------------------------------|---------------------|
| SWCNTs/ Fe_xO_y | 191 | 0.389 | 4.314 |
| As-grown SWCNTs | 115 | 0.299 | 3.828 |

Figure 5a is the hysteresis loop of the SWCNTs/ Fe_xO_y . The coercivity and remanence of the SWCNTs/ Fe_xO_y are both zero, indicating the paramagnetic nature of this nanocomposite material. The saturation magnetization strength at room temperature is measured at 33.32 emu/g, suggesting that this material is capable of achieving solid–liquid separation. Figure 5b is a photo of a small experiment in which magnetic SWCNTs/ Fe_xO_y can be rapidly collected in a BPA solution with a concentration of 0.25 mmol/L using magnets.

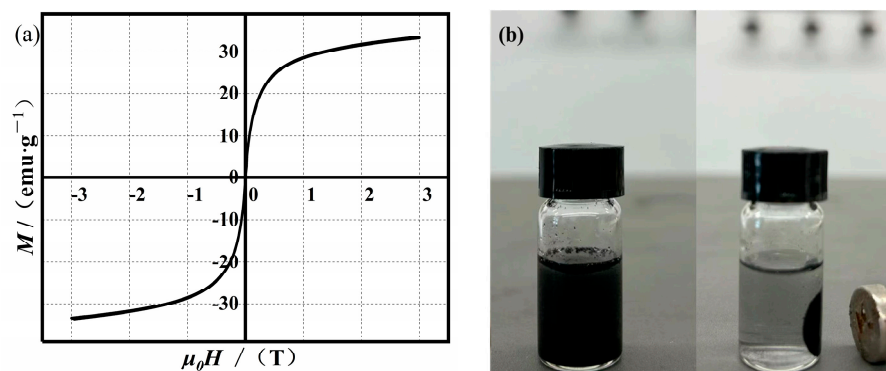


Figure 5. (a) Hysteresis loop of SWCNTs/ Fe_xO_y and (b) a photo of a small experiment.

3.2. Adsorption Studies

Under the conditions of $T = 25 \text{ }^\circ\text{C}$, $\text{pH} = 6$, the adsorption rate of the as-grown SWCNTs and SWCNTs/ Fe_xO_y on BPA was studied. As depicted in Figure 6, the adsorption rate of BPA by both nanocomposites increased with time. Both adsorbents reached equilibrium within 15 min, with the SWCNTs/ Fe_xO_y exhibiting an equilibrium adsorption rate of 97%, which represents a 50% improvement over the as-grown SWCNTs, indicating that the heat-treated composites exhibited a superior adsorption performance. Consequently, further experiments will utilize SWCNTs/ Fe_xO_y as the adsorbent for research purposes.

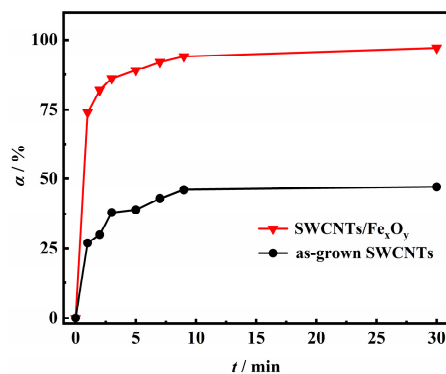


Figure 6. As-grown SWCNTs and SWCNTs/Fe_xO_y adsorption curves ($T = 25\text{ }^{\circ}\text{C}$, $\text{pH} = 6$, adsorbent dosage = 0.2 g/L , $C_{\text{BPA}} = 0.025\text{ mmol/L}$).

Figure 7 illustrates the relationship between the rate of adsorption of BPA and the absorption time under different starting concentrations of BPA. Solutions of varying concentrations reached adsorption equilibrium within 15 min, and the starting concentration significantly influenced the BPA equilibrium adsorption rate. The adsorption rate decreased as the initial BPA concentration increased. When the concentration of the BPA solution increased from 0.025 to 0.15 mmol/L, the equilibrium adsorption rate decreased from 98% to 51%. This reduction is primarily due to the limited adsorption capacity of the SWCNTs/Fe_xO_y towards BPA. Exceeding the adsorption capacity of the SWCNTs/Fe_xO_y with a high initial concentration of BPA solution results in the adsorption of merely a fraction of the BPA molecules. Within the initial 0–10 min, the adsorption rate of the SWCNTs/Fe_xO_y increased rapidly, followed by a slower progression. This phenomenon can be attributed to the initial abundance of adsorption sites on the adsorbent, which allowed for the rapid adsorption of BPA from the solution. As adsorption continued, these sites became gradually saturated with BPA molecules, reducing the pore transport capacity and leading to a gradual decrease in the adsorption efficiency until equilibrium was reached. Furthermore, it was observed that for BPA at low concentrations, such as concentrations of 0.025 and 0.05 mmol/L, an adsorption rate of 90% can be achieved after 5 min. Hence, the SWCNT composite loaded with iron oxide nanoparticles can be considered a rapid and effective adsorbent for BPA, especially at lower concentrations.

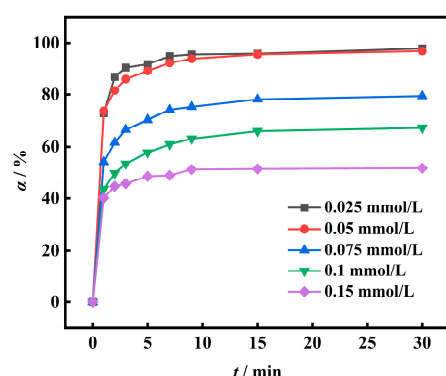


Figure 7. Effect of different initial concentrations ($T = 25\text{ }^{\circ}\text{C}$, $\text{pH} = 6$, adsorbent dosage = 0.2 g/L).

The relationship between the removal rate of BPA and the dosage of the SWCNTs/Fe_xO_y is depicted in Figure 8, with the dosage ranging from 0.05 to 0.35 g/L. An adsorbent dosage of 0.05 g/L resulted in a BPA adsorption rate of 34%. As the adsorbent dosage increased to 0.3 g/L, the adsorption rate reached 96.8% and, upon further increment to 0.35 g/L, exhibited little change, remaining at approximately 97%. Nonetheless, an increment in the adsorbent dosage resulted in a diminution of the adsorption capacity. This phenomenon can be attributed to the fact that while the adsorbent dosage increased,

the amount of adsorbate remained unchanged, resulting in an excess of the adsorbent competing with the BPA molecules. At the same time, excessive adsorbents caused the overlap of effective adsorption sites on SWCNTs/Fe_xO_y, consequently reducing the BPA content per unit mass of the adsorbent.

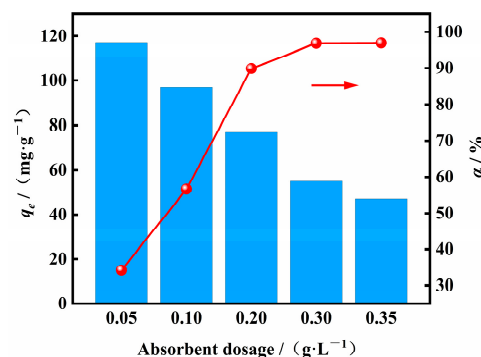


Figure 8. Effect of adsorbent dosage ($T = 25\text{ }^{\circ}\text{C}$, $\text{pH} = 6$, $C_{\text{BPA}} = 0.075\text{ mmol/L}$).

3.3. Effect of pH Value on Adsorption

The acid or base nature of a solution exerts influence not merely on the solubility of the adsorbent but also affects the speciation of ions within the solution. To investigate the effect of pH on adsorption, the pH of a 0.15 mmol/L BPA solution was adjusted using HCl or NaOH. This was conducted at an adsorption temperature of 25 °C and an adsorbent dosage of 0.2 g/L. As Figure 9a illustrates, the adsorption rate of BPA decreased with increasing pH. At acidic pH (pH = 3), the nanocomposite exhibited an adsorption rate of 68% towards a BPA solution with $C_0 = 0.15\text{ mmol/L}$. Under neutral and alkaline conditions, the adsorption rates were 56% and 50%, respectively. The maximum adsorption rate was observed at pH = 3, and the adsorption capacity of the SWCNTs/Fe_xO_y for BPA gradually diminished as the pH value increased. Therefore, for practical applications, wastewater acidification is often used as a pre-treatment step for adsorption methods. This process can break down complex polymeric organic matter into smaller molecular organic compounds, but the acidification of wastewater will also increase the cost and affect the biological treatment.

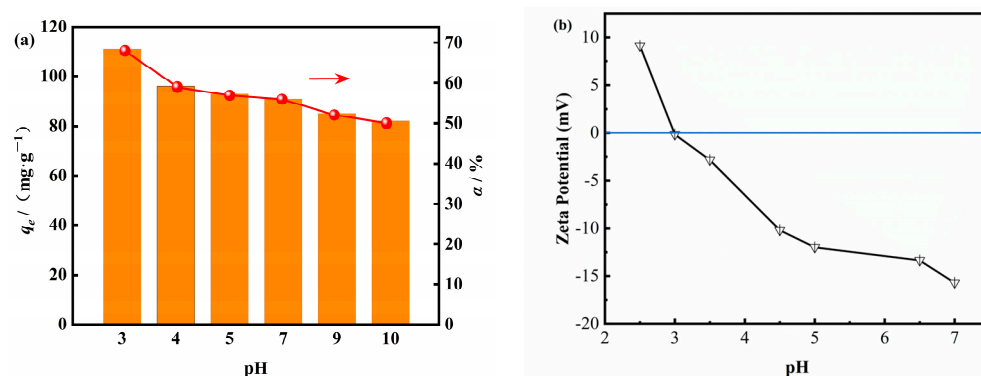


Figure 9. (a) Effect of pH value and (b) the point of zero charge of SWCNTs/Fe_xO_y.

In general, BPA is present in its molecular form in the solution. However, the deprotonation of the BPA single anion occurs at pH 8, and further ionization occurs when the pH exceeds 9.6. Additionally, we also identified the point zero charge (pH_{pzc}) of the SWCNTs/Fe_xO_y in the study, which is about 2.9, so the nanocomposite is positively charged at a pH below 2.9 and negatively charged at a pH above 2.9. Therefore, BPA²⁻ and negatively charged SWCNTs experienced electrostatic repulsion [32], which resulted in a decrease in the adsorption rate of BPA onto the SWCNTs/Fe_xO_y as pH increased. Moreover, it is evident that the electrostatic interaction between the BPA and SWCNTs/Fe_xO_y is not the primary factor controlling adsorption.

3.4. Adsorption Isotherm

An adsorption isotherm describes the relationship between the equilibrium concentration of a solution and the corresponding equilibrium adsorption capacity, which is attained when the adsorption process reaches equilibrium at a given temperature. To model this equilibrium, two widely used isotherm equations, the Langmuir [33] and Freundlich [34] models, are often employed to fit experimental data. The mathematical expressions for these models are as follows:

$$q_e = \frac{K_L q_{max} C_e}{1 + K_L C_e}, \quad (3)$$

$$q_e = K_F C_e^{\frac{1}{n}}, \quad (4)$$

where q_e is the adsorption capacity of the unit adsorbent to BPA at the adsorption equilibrium (mg/g); C_e is the concentration of BPA in solution at equilibrium (mmol/L); q_{max} is the theoretical maximum adsorption capacity (mg/g); and K_L , K_F , and n are all model constants. The value of n serves as an indicator of the ease or difficulty associated with the adsorption process. Adsorption is more likely to occur when the value of n is within the range of 1 to 10.

The data on the adsorption of BPA by the SWCNTs/Fe_xO_y were also analyzed using the Dubinin–Radushkevich (D-R) adsorption isotherm model. The mathematical expressions for the model are as follows:

$$q_e = q_{max} \exp \left[-\beta \left\{ RT \ln \left(1 + \frac{1}{C_e} \right) \right\}^2 \right], \quad (5)$$

$$\varepsilon = RT \ln \left(1 + \frac{1}{C_e} \right), \quad (6)$$

$$E_a = \frac{1}{\sqrt{2\beta}}, \quad (7)$$

where q_{max} is the maximum adsorption capacity calculated according to the D-R model, mg·g⁻¹; β is a constant related to the adsorption energy E_a (kJ·mol⁻¹), mol²·kJ⁻²; ε is the Polanyi adsorption potential. When the E_a value is in the range of 1–8 kJ·mol⁻¹, it indicates physical adsorption. When the E_a value exceeds 8 kJ·mol⁻¹, chemisorption is predominant.

Figure 10 illustrates the Langmuir, Freundlich, and D-R adsorption isotherms associated with the removal of BPA from solution using SWCNTs/Fe_xO_y. The corresponding fitting parameters were presented in Table 2. The data demonstrate a better fit with the Langmuir and D-R isotherm models, as indicated by the correlation fitting coefficient (R^2) values of 0.903 and 0.913, respectively, compared to the R^2 value of 0.874 for the Freundlich model. This implies that the BPA molecules are likely adsorbed onto the SWCNTs/Fe_xO_y in a uniform monolayer. The maximum adsorption capacity as determined by the Langmuir model is 78.89 mg/g. The BPA adsorption energy calculated using the D-R model is 1.543 kJ/mol, indicating that the adsorption process is predominantly physical adsorption. As indicated in the table, the value of n is 5.559, suggesting that the adsorption process occurs easily.

Table 2. Fitting parameters of isothermal adsorption models.

| Langmuir | | | Freundlich | | | Dubinin–Radushkevich (D-R) | | | |
|------------------------------------|--------------------------------|-------|------------|-------|-------|------------------------------------|--|----------------------------------|-------|
| q_{max} (mg·g ⁻¹) | K_L (L·mg ⁻¹) | R^2 | K_F | n | R^2 | q_{max} (mg·g ⁻¹) | β (mol ² ·kJ ⁻²) | E_a (kJ·mol ⁻¹) | R^2 |
| 78.89 | 4.714 | 0.903 | 52.68 | 5.559 | 0.874 | 76.22 | 0.20989 | 1.543 | 0.913 |

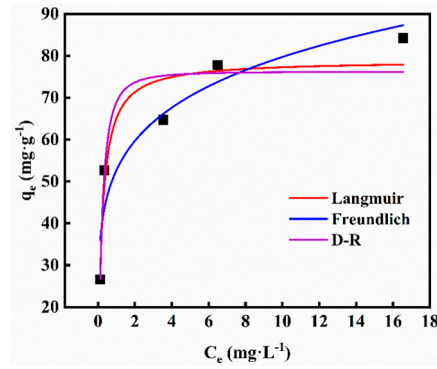


Figure 10. Langmuir, Freundlich, and D-R adsorption isotherms ($T = 25\text{ }^{\circ}\text{C}$, $\text{pH} = 6$, adsorbent dosage = 0.2 g/L).

3.5. Adsorption Kinetics

In this study, the adsorption rate and mechanism of SWCNTs/ Fe_xO_y adsorbing BPA were examined by fitting the data to pseudo first-order and pseudo second-order kinetic models. The equations for these two adsorption kinetic models are as follows [35]:

$$q_t = q_e \left(1 - e^{-k_1 t}\right), \tag{8}$$

$$\frac{t}{q_t} = \frac{1}{k_2 q_e^2} + \frac{1}{q_e} t, \tag{9}$$

where q_t is the adsorption capacity of the unit adsorbent to the BPA at time t (mg/g); q_e is the adsorption capacity of the unit adsorbent to BPA at adsorption equilibrium (mg/g); k_1 and k_2 are both adsorption rate constants.

Figure 11a,b illustrate the kinetic fittings of the SWCNTs/ Fe_xO_y for the BPA solutions with varying initial concentrations. The corresponding kinetic fitting parameters are listed in Table 3. The data demonstrate that the second-order kinetics model fits the experimental data of BPA better than the first-order kinetic model, with the correlation coefficients (R^2) exceeding 0.99 in both cases. The equilibrium adsorption capacity, as calculated from the pseudo second-order kinetic curves, is closer to the experimental values, suggesting that chemisorption was the primary mechanism driving the adsorption process. The adsorption mechanism was likely influenced by various forces, such as π - π electron donor–acceptor interactions, hydrogen bonding, etc.

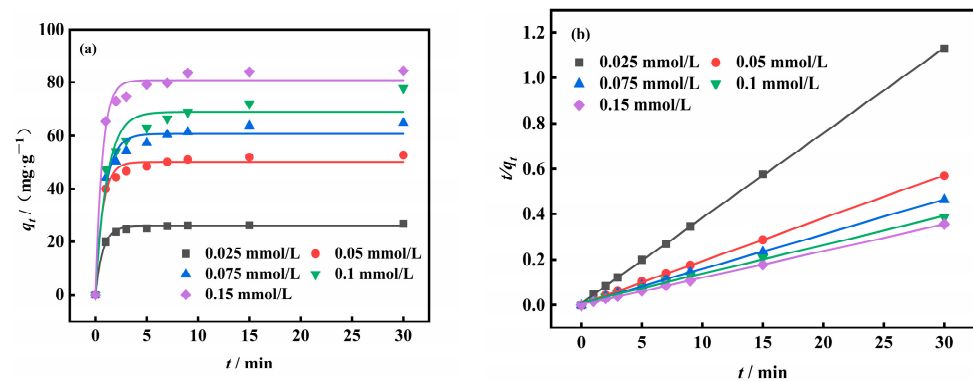


Figure 11. Kinetic fitting curves: (a) pseudo first-order kinetics; (b) pseudo second-order kinetic ($T = 25\text{ }^{\circ}\text{C}$, $\text{pH} = 6$, adsorbent dosage = 0.2 g/L).

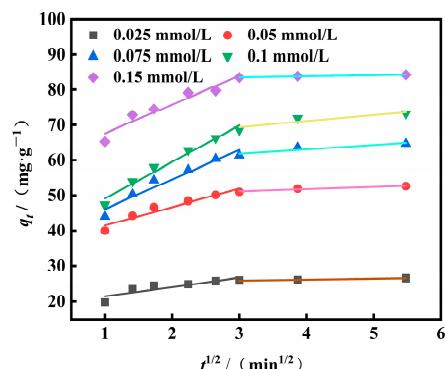
Table 3. Fitting parameters of kinetics.

| C_0 $\text{mmol}\cdot\text{L}^{-1}$ | Pseudo First-Order | | | Pseudo Second-Order | | |
|--|----------------------------|--|--------|--|--|--------|
| | k_1 min^{-1} | q_e $\text{mg}\cdot\text{g}^{-1}$ | R^2 | k_2 $\text{g}\cdot\text{mg}^{-1}\cdot\text{min}^{-1}$ | q_e $\text{mg}\cdot\text{g}^{-1}$ | R^2 |
| 0.025 | 1.40 | 25.69 | 0.9950 | 0.14 | 26.75 | 0.9998 |
| 0.05 | 1.43 | 50.08 | 0.9830 | 0.06 | 53.16 | 0.9998 |
| 0.075 | 1.08 | 60.69 | 0.9724 | 0.03 | 65.62 | 0.9994 |
| 0.1 | 0.90 | 68.77 | 0.9422 | 0.01 | 78.86 | 0.9969 |
| 0.15 | 1.50 | 80.71 | 0.9834 | 0.04 | 85.03 | 0.9997 |

To further elucidate the principal mechanism governing the adsorption process, the Weber–Morris model [36] was employed to fit the data depicted in Figure 12.

$$q_t = k_{int}t^{1/2} + I, \quad (10)$$

where k_{int} is the intraparticle diffusion rate constant. The value I represents the boundary layer thickness, i.e., the larger the intercept, the greater the boundary layer effect will be [37]. According to this model, if the fitting line of q_t and $t^{1/2}$ passes through the origin, then the internal diffusion of the particle determines the adsorption rate.

**Figure 12.** Weber–Morris curves ($T = 25\text{ }^{\circ}\text{C}$, $\text{pH} = 6$, adsorbent dosage = 0.2 g/L).

The relationship between q_t and $t^{1/2}$ was observed to be nonlinear, indicating a multi-line relationship. The adsorption process can be divided into two stages: Firstly, there is the rapid adsorption stage, which is considered to be the swift diffusion of the adsorbate to the surface of the adsorbent; the SWCNTs/ Fe_xO_y contain abundant π electrons, which form π - π conjugations [38] with π electrons in the benzene ring in the structure of BPA. In the early stages of adsorption, the SWCNTs/ Fe_xO_y had a larger specific surface area and numerous available adsorption sites, allowing for more π electrons to be exposed for binding with BPA. Consequently, the rate of adsorption of BPA increased rapidly with the adsorption time. The second stage was a slower adsorption phase, where the BPA molecules diffused into the mesopore and macropore of the SWCNTs/ Fe_xO_y . As the BPA concentration decreased, the number of effective adsorption sites on the SWCNTs/ Fe_xO_y also diminished, and the quantity of BPA molecules within the adsorbent gradually increased. Adsorption was influenced by the concentration and molecular size of the adsorbate. As adsorption approached equilibrium, the diffusion resistance rose. The fact that $I \neq 0$ under the test conditions suggested that intra-particle diffusion was not the sole rate-limiting step, and that several other controlling factors significantly influenced the adsorption of BPA by the CNTs.

3.6. Comparison of Adsorption Quantity

The adsorption capacity of the SWCNTs/ Fe_xO_y composites for the removal of BPA, as illustrated in this study, was comparatively assessed with data from other adsorbents reported in the literature, with the findings being summarized in Table 4. Figure 13 shows

the adsorption mechanism of the SWCNTs/Fe_xO_y for BPA. Combined with Table 4 and Figure 13, it can be seen that the modified SWCNTs/Fe_xO_y had an excellent adsorption capacity for BPA. Previous studies have suggested that the two phenyl rings of the BPA molecule can be adsorbed onto the surface of CNTs in various configurations: namely, aligned parallel to the longitudinal axis of the tube, encircling the circumference, or positioned diagonally. This adsorption is purported to occur via a π - π electron donor–acceptor interaction, culminating in the establishment of a π - π conjugation with the π electron system of the CNTs. Furthermore, it has been suggested that the reliance of these π - π interactions on pH is minimal, indicating a robustness in the adsorption mechanism across varying pH conditions. In this research, the modification of the SWCNTs results in a larger surface area and the presence of numerous micropores and mesopores, which allows for more π electrons to be exposed for binding with BPA and to form π - π conjugations, thus accelerating the adsorption process. Furthermore, the hydrophobic nature of the carbon nanotube surfaces [39,40] has been found to be effective in BPA adsorption, exhibiting a pH independence similar to that of π - π interactions. Additionally, the water solubility of BPA should be considered; in alkaline conditions, BPA exists in a salt form, which can also affect adsorption. Finally, the unique magnetic properties of the SWCNTs/Fe_xO_y are expected to facilitate the recovery and reuse of the adsorbent, minimizing the potential harm to humans or aquatic organisms.

Table 4. The adsorption capacity of BPA by SWCNTs observed in this work is compared with that reported for other adsorbents in the literature.

| Target Adsorbate | Adsorbent | pH Value | Maximum Capacity (mg·g ⁻¹) | References |
|------------------|---|----------|--|------------|
| BPA | N-NiO@N-Fe ₃ O ₄ @N-ZnO | 5 | 100 | [41] |
| BPA | activated carbon | 7 | 44.1 | [42] |
| BPA | MWCNTs/SiO ₂ /CS | 6.22 | 46.2 | [43] |
| BPA | HMWCNTs/Fe ₃ O ₄ | - | 113 | [44] |
| BPA | MWCNTs/Fe ₃ O ₄ | 6.2 | 45.31 | [27] |
| BPA | Fe ₃ O ₄ /GO | - | 72.8 | [45] |
| BPA | SWCNTs/Fe _x O _y | 3 | 117 | This work |
| | | 4 | 96 | This work |
| | | 5 | 93 | This work |
| | | 7 | 91 | This work |

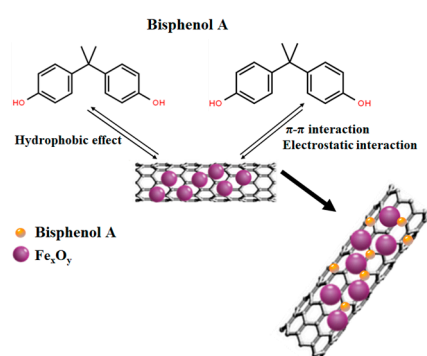


Figure 13. The main mechanism of adsorption of SWCNTs/Fe_xO_y on BPA.

4. Conclusions

In this work, high-quality SWCNTs containing an iron catalyst were prepared by a simple arc discharge method in a hydrogen–argon mixed atmosphere, and the iron nanoparticles were oxidized in situ into magnetic iron oxide nanoparticles by air heat treatment. Based on the unique structure of this nanocomposite material, the adsorption performance of BPA in water as an adsorbent was studied. The main findings are as follows:

- (1) At the same pH value, compared to other CNTs or carbon materials coated with different oxides, this composite material demonstrates a higher efficiency in adsorbing BPA. After air heat treatment, the SWCNT composite material possesses an increased surface area, which enhances its adsorption efficiency.
- (2) At low initial BPA concentrations, especially below 0.05 mmol/L, the adsorption efficiency quickly reaches 90% and quickly reaches equilibrium. Acidic conditions were more conducive to the adsorption of BPA by SWCNTs/Fe_xO_y.
- (3) The kinetic calculations of adsorption indicate that the process follows a pseudo second-order kinetic model. The experimental data fit well with the Langmuir and D-R adsorption isotherm models. Therefore, the adsorption of BPA on the SWCNTs/Fe_xO_y is likely to be in the form of a uniform monolayer, and the adsorption process is more consistent with physical adsorption.

The nanocomposite not only exhibits excellent adsorption capacity for hydrophobic phenols (BPA) but also exhibits effective magnetic separation performance, and is easy to recover from water, so it is a promising material for removing BPA from water. Its adsorption capacity is higher under acidic conditions, so the next step will be to study its adsorption performance in actual wastewater. We also need to pay attention to the effect of the Fe doping ratio on adsorption.

Author Contributions: Conceptualization, L.C.; methodology, L.C., J.J. and L.S.; software, L.C.; validation, L.C. and J.J.; formal analysis, L.C.; investigation, L.C. and J.J.; resources, L.S.; data curation, L.C. and J.J.; writing—original draft preparation, L.C.; writing—review and editing, L.S. and J.J.; visualization, L.C.; supervision, L.S.; project administration, L.S.; funding acquisition, L.S. All authors have read and agreed to the published version of the manuscript.

Funding: This work was financially supported by the Foundation Strengthening Program Project Fund (No. 2020-JCJQ-JJ-417).

Institutional Review Board Statement: Not applicable.

Informed Consent Statement: Not applicable.

Data Availability Statement: The data presented in this study are available on request from the corresponding author.

Conflicts of Interest: The authors declare no conflicts of interest.

References

1. Jin, H.; Zhu, L. Occurrence and partitioning of bisphenol analogues in water and sediment from Liaohe River Basin and Taihu Lake, China. *Water Res.* **2016**, *103*, 343–351. [[CrossRef](#)] [[PubMed](#)]
2. Wu, D.; He, L.; Sun, R.; Tong, M.; Kim, H. Influence of Bisphenol A on the transport and deposition behaviors of bacteria in quartz sand. *Water Res.* **2017**, *121*, 1–10. [[CrossRef](#)] [[PubMed](#)]
3. Yuan, M.; Chen, S.; Zeng, C.; Fan, Y.; Ge, W.; Chen, W. Estrogenic and non-estrogenic effects of bisphenol A and its action mechanism in the zebrafish model: An overview of the past two decades of work. *Environ. Int.* **2023**, *176*, 107976. [[CrossRef](#)] [[PubMed](#)]
4. Cimmino, I.; Fiory, F.; Perruolo, G.; Miele, C.; Beguinot, F.; Formisano, P.; Oriente, F. Potential Mechanisms of Bisphenol A (BPA) Contributing to Human Disease. *Int. J. Mol. Sci.* **2020**, *21*, 5761. [[CrossRef](#)] [[PubMed](#)]
5. Adebawale, K.O.; Egbadina, A.O. Facile green synthesis of bio-carbon material from eggshells and its application for the removal of Bisphenol A and 2,4,6-trichlorophenol from water. *Environ. Nanotechnol. Monit. Manag.* **2022**, *17*, 100622. [[CrossRef](#)]
6. Modi, A.; Bellare, J. Copper sulfide nanoparticles/carboxylated graphene oxide nanosheets blended polyethersulfone hollow fiber membranes: Development and characterization for efficient separation of oxybenzone and bisphenol A from water. *Polymer* **2019**, *163*, 57–67. [[CrossRef](#)]
7. Huang, Y.; Yang, T.; Liang, M.; Wang, Y.; Xu, Z.; Zhang, D.; Li, L. Ni-Fe layered double hydroxides catalyzed ozonation of synthetic wastewater containing Bisphenol A and municipal secondary effluent. *Chemosphere* **2019**, *235*, 143–152. [[CrossRef](#)]
8. Yue, W.; Yin, C.-F.; Sun, L.; Zhang, J.; Xu, Y.; Zhou, N.-Y. Biodegradation of bisphenol-A polycarbonate plastic by *Pseudomonas* sp. strain NyZ600. *J. Hazard. Mater.* **2021**, *416*, 125775. [[CrossRef](#)]
9. Dehghani, M.H.; Ghadermazi, M.; Bhatnagar, A.; Sadighara, P.; Jahed-Khaniki, G.; Heibati, B.; McKay, G. Adsorptive removal of endocrine disrupting bisphenol A from aqueous solution using chitosan. *J. Environ. Chem. Eng.* **2016**, *4*, 2647–2655. [[CrossRef](#)]

10. Li, Y.; Zhu, H.; Zhang, C.; Cheng, M.; He, H. PEI-grafted magnetic cellulose for Cr(VI) removal from aqueous solution. *Cellulose* **2018**, *25*, 4757–4769. [[CrossRef](#)]
11. Kah, M.; Sigmund, G.; Xiao, F.; Hofmann, T. Sorption of ionizable and ionic organic compounds to biochar, activated carbon and other carbonaceous materials. *Water Res.* **2017**, *124*, 673–692. [[CrossRef](#)] [[PubMed](#)]
12. Jabeen, A.; Kamran, U.; Noreen, S.; Park, S.-J.; Bhatti, H.N. Mango seed-derived hybrid composites and sodium alginate beads for the efficient uptake of 2,4,6-trichlorophenol from simulated wastewater. *Catalysts* **2022**, *12*, 972. [[CrossRef](#)]
13. Kamran, U.; Bhatti, H.N.; Noreen, S.; Tahir, M.A.; Park, S.-J. Chemically modified sugarcane bagasse-based biocomposites for efficient removal of acid red 1 dye: Kinetics, isotherms, thermodynamics, and desorption studies. *Chemosphere* **2022**, *291*, 132796. [[CrossRef](#)] [[PubMed](#)]
14. Mariyam, A.; Mittal, J.; Sakina, F.; Baker, R.T.; Sharma, A.K.; Mittal, A. Efficient batch and Fixed-Bed sequestration of a basic dye using a novel variant of ordered mesoporous carbon as adsorbent. *Arab. J. Chem.* **2021**, *14*, 103186. [[CrossRef](#)]
15. Mishakov, I.V.; Bauman, Y.I.; Brzhezinskaya, M.; Netskina, O.V.; Shubin, Y.V.; Kibis, L.S.; Stoyanovskii, V.O.; Larionov, K.B.; Serkova, A.N.; Vedyagin, A.A. Water purification from chlorobenzenes using heteroatom-functionalized carbon nanofibers produced on self-organizing Ni-Pd catalyst. *J. Environ. Chem. Eng.* **2022**, *10*, 107873. [[CrossRef](#)]
16. Rahman, G.; Najaf, Z.; Mehmood, A.; Bilal, S.; Shah, A.U.H.A.; Mian, S.A.; Ali, G. An overview of the recent progress in the synthesis and applications of carbon nanotubes. *C* **2019**, *5*, 3. [[CrossRef](#)]
17. Krishna, R.H.; Chandraprabha, M.; Samrat, K.; Murthy, T.K.; Manjunatha, C.; Kumar, S.G. Carbon nanotubes and graphene-based materials for adsorptive removal of metal ions—a review on surface functionalization and related adsorption mechanism. *Appl. Surf. Sci. Adv.* **2023**, *16*, 100431. [[CrossRef](#)]
18. Pan, B.; Xing, B. Adsorption mechanisms of organic chemicals on carbon nanotubes. *Environ. Sci. Technol.* **2008**, *42*, 9005–9013. [[CrossRef](#)] [[PubMed](#)]
19. Kang, S.; Herzberg, M.; Rodrigues, D.F.; Elimelech, M. Antibacterial Effects of Carbon Nanotubes: Size Does Matter! *Langmuir* **2008**, *24*, 6409–6413. [[CrossRef](#)]
20. Donadelli, J.A.; Carlos, L.; Arques, A.; Einschlag, F.S.G. Kinetic and mechanistic analysis of azo dyes decolorization by ZVI-assisted Fenton systems: pH-dependent shift in the contributions of reductive and oxidative transformation pathways. *Appl. Catal. B* **2018**, *231*, 51–61. [[CrossRef](#)]
21. Wang, H.; Jia, S.; Wang, H.; Li, B.; Liu, W.; Li, N.; Qiao, J.; Li, C.-Z. A novel-green adsorbent based on betaine-modified magnetic nanoparticles for removal of methyl blue. *Sci. Bull.* **2017**, *62*, 319–325. [[CrossRef](#)] [[PubMed](#)]
22. Yadav, A.; Bagotia, N.; Yadav, S.; Sharma, A.K.; Kumar, S. In-situ fabrication of surfactant modified CNT-based novel bio-composite and its performance evaluation for simultaneous removal of anionic dyes: Optimization by Box-Behnken design. *Sep. Purif. Technol.* **2022**, *284*, 120262. [[CrossRef](#)]
23. Sarkar, B.; Mandal, S.; Tsang, Y.F.; Kumar, P.; Kim, K.-H.; Ok, Y.S. Designer carbon nanotubes for contaminant removal in water and wastewater: A critical review. *Sci. Total Environ.* **2018**, *612*, 561–581. [[CrossRef](#)] [[PubMed](#)]
24. Mou, F.; Guan, J.; Xiao, Z.; Sun, Z.; Shi, W.; Fan, X.-A. Solvent-mediated synthesis of magnetic Fe₂O₃ chestnut-like amorphous-core/ γ -phase-shell hierarchical nanostructures with strong As (v) removal capability. *J. Mater. Chem.* **2011**, *21*, 5414–5421. [[CrossRef](#)]
25. Cuzzola, A.; Bernini, M.; Salvadori, P. A preliminary study on iron species as heterogeneous catalysts for the degradation of linear alkylbenzene sulphonic acids by H₂O₂. *Appl. Catal. B* **2002**, *36*, 231–237. [[CrossRef](#)]
26. Munoz, M.; de Pedro, Z.M.; Casas, J.A.; Rodriguez, J.J. Preparation of magnetite-based catalysts and their application in heterogeneous Fenton oxidation—A review. *Appl. Catal. B* **2015**, *176*, 249–265. [[CrossRef](#)]
27. Li, S.; Gong, Y.; Yang, Y.; He, C.; Hu, L.; Zhu, L.; Sun, L.; Shu, D. Recyclable CNTs/Fe₃O₄ magnetic nanocomposites as adsorbents to remove bisphenol A from water and their regeneration. *Chem. Eng. J.* **2015**, *260*, 231–239. [[CrossRef](#)]
28. Al-Musawi, T.J.; Mengelizadeh, N.; Ganji, F.; Wang, C.; Balarak, D. Preparation of multi-walled carbon nanotubes coated with CoFe₂O₄ nanoparticles and their adsorption performance for Bisphenol A compound. *Adv. Powder Technol.* **2022**, *33*, 103438. [[CrossRef](#)]
29. Guo, X.; Huang, Y.; Yu, W.; Yu, X.; Han, X.; Zhai, H. Multi-walled carbon nanotubes modified with iron oxide and manganese dioxide (MWCNTs-Fe₃O₄-MnO₂) as a novel adsorbent for the determination of BPA. *Microchem. J.* **2020**, *157*, 104867. [[CrossRef](#)]
30. Xu, G.; Zhang, B.; Wang, X.; Li, N.; Liu, L.; Lin, J.-M.; Zhao, R.-S. Nitrogen-doped flower-like porous carbon nanostructures for fast removal of sulfamethazine from water. *Environ. Pollut.* **2019**, *255*, 113229. [[CrossRef](#)]
31. Zhao, X.; Inoue, S.; Jinno, M.; Suzuki, T.; Ando, Y. Macroscopic oriented web of single-wall carbon nanotubes. *Chem. Phys. Lett.* **2003**, *373*, 266–271. [[CrossRef](#)]
32. Yu, F.; Sun, S.; Han, S.; Zheng, J.; Ma, J. Adsorption removal of ciprofloxacin by multi-walled carbon nanotubes with different oxygen contents from aqueous solutions. *Chem. Eng. J.* **2016**, *285*, 588–595. [[CrossRef](#)]
33. Athalathil, S.; Stüber, F.; Bengoa, C.; Font, J.; Fortuny, A.; Fabregat, A. Characterization and performance of carbonaceous materials obtained from exhausted sludges for the anaerobic biodecolorization of the azo dye Acid Orange II. *J. Hazard. Mater.* **2014**, *267*, 21–30. [[CrossRef](#)] [[PubMed](#)]
34. Joseph, L.; Boateng, L.K.; Flora, J.R.; Park, Y.-G.; Son, A.; Badawy, M.; Yoon, Y. Removal of bisphenol A and 17 α -ethinyl estradiol by combined coagulation and adsorption using carbon nanomaterials and powdered activated carbon. *Sep. Purif. Technol.* **2013**, *107*, 37–47. [[CrossRef](#)]

35. Zhang, S.; Shao, T.; Kose, H.S.; Karanfil, T. Adsorption kinetics of aromatic compounds on carbon nanotubes and activated carbons. *Environ. Toxicol. Chem.* **2012**, *31*, 79–85. [[CrossRef](#)] [[PubMed](#)]
36. Faria, M.C.; Rosemberg, R.S.; Bomfeti, C.A.; Monteiro, D.S.; Barbosa, F.; Oliveira, L.C.; Rodriguez, M.; Pereira, M.C.; Rodrigues, J.L. Arsenic removal from contaminated water by ultrafine δ -FeOOH adsorbents. *Chem. Eng. J.* **2014**, *237*, 47–54. [[CrossRef](#)]
37. Mane, V.S.; Mall, I.D.; Srivastava, V.C. Kinetic and equilibrium isotherm studies for the adsorptive removal of Brilliant Green dye from aqueous solution by rice husk ash. *J. Environ. Manag.* **2007**, *84*, 390–400. [[CrossRef](#)] [[PubMed](#)]
38. Sun, Z.; Zhao, L.; Liu, C.; Zhen, Y.; Ma, J. Fast adsorption of BPA with high capacity based on π - π electron donor-acceptor and hydrophobicity mechanism using an in-situ sp^2 C dominant N-doped carbon. *Chem. Eng. J.* **2020**, *381*, 122510. [[CrossRef](#)]
39. Xiao, P.; Wang, P.; Li, H.; Li, Q.; Shi, Y.; Wu, X.-L.; Lin, H.; Chen, J.; Wang, X. New insights into bisphenols removal by nitrogen-rich nanocarbons: Synergistic effect between adsorption and oxidative degradation. *J. Hazard. Mater.* **2018**, *345*, 123–130. [[CrossRef](#)]
40. Oyetade, O.A.; Martincigh, B.S.; Skelton, A.A. Interplay between electrostatic and hydrophobic interactions in the pH-dependent adsorption of ibuprofen onto acid-functionalized multiwalled carbon nanotubes. *J. Phys. Chem. C* **2018**, *122*, 22556–22568. [[CrossRef](#)]
41. Allam, E.A.; Ali, A.S.M.; Elsharkawy, R.M.; Mahmoud, M.E. Framework of nano metal oxides N-NiO@N-Fe₃O₄@N-ZnO for adsorptive removal of atrazine and bisphenol-A from wastewater: Kinetic and adsorption studies. *Environ. Nanotechnol. Monit. Manag.* **2021**, *16*, 100481. [[CrossRef](#)]
42. Bautista-Toledo, I.; Ferro-García, M.; Rivera-Utrilla, J.; Moreno-Castilla, C.; Vegas Fernández, F. Bisphenol A removal from water by activated carbon. Effects of carbon characteristics and solution chemistry. *Environ. Sci. Technol.* **2005**, *39*, 6246–6250. [[CrossRef](#)] [[PubMed](#)]
43. Mohammadi, A.A.; Dehghani, M.H.; Mesdaghinia, A.; Yaghmaian, K.; Es'haghi, Z. Adsorptive removal of endocrine disrupting compounds from aqueous solutions using magnetic multi-wall carbon nanotubes modified with chitosan biopolymer based on response surface methodology: Functionalization, kinetics, and isotherms studies. *Int. J. Biol. Macromol.* **2020**, *155*, 1019–1029. [[CrossRef](#)] [[PubMed](#)]
44. Gao, H.; Han, X.; Wang, R.; Zhu, K.; Han, R. Adsorption and catalytic degradation of bisphenol A and p-chlorophenol by magnetic carbon nanotubes. *Environ. Res.* **2023**, *231*, 116314. [[CrossRef](#)]
45. Ouyang, K.; Zhu, C.; Zhao, Y.; Wang, L.; Xie, S.; Wang, Q. Adsorption mechanism of magnetically separable Fe₃O₄/graphene oxide hybrids. *Appl. Surf. Sci.* **2015**, *355*, 562–569. [[CrossRef](#)]

Disclaimer/Publisher's Note: The statements, opinions and data contained in all publications are solely those of the individual author(s) and contributor(s) and not of MDPI and/or the editor(s). MDPI and/or the editor(s) disclaim responsibility for any injury to people or property resulting from any ideas, methods, instructions or products referred to in the content.